SUPPLEMENTARY MATERIAL FOR THE PAPER:

Crystal Growth According to the Law of Proportionate Effect

by D. D. Eberl

(Figures can be expanded for easier viewing)

Badino, G., Ferreira, A., Forti, P., Giovani, P., Giulivo, I, Infanti3, G., Lo Mastro, F., Sanna, L., and Tedeschi, R. (2009) The Nasca caves survey. Fifteenth International Congress of Speleology At: Kerrville, Texas, 1764-17869.

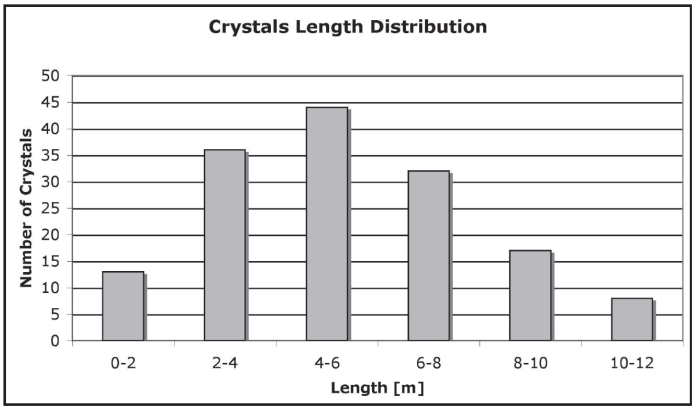

Figure 5: Cristales, distribution of crystals lengths.

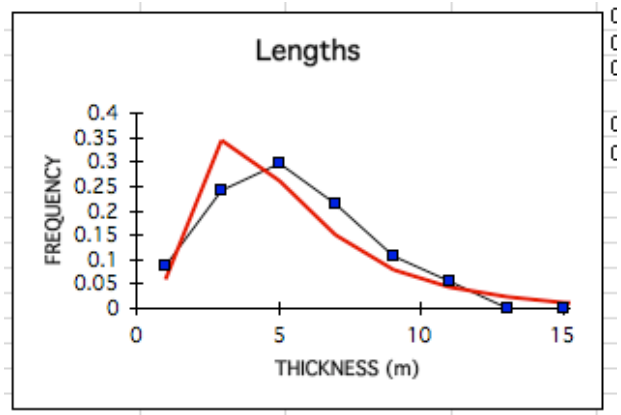

MEAN SIZE=	5.35
ALPHA=	1.523
BETA^2=	0.376

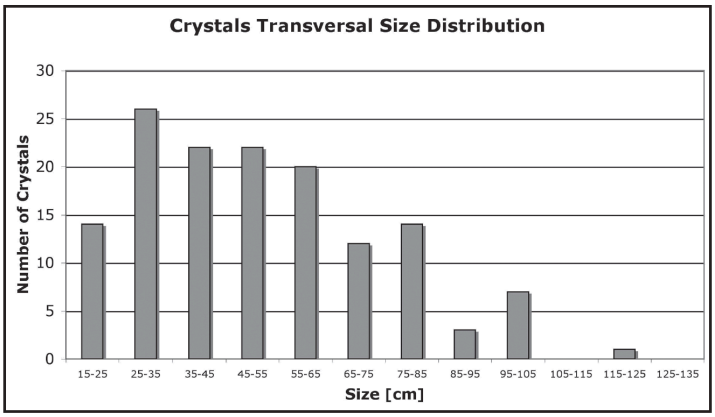

Figure 7: Cristales, distribution of crystals transversal sizes.

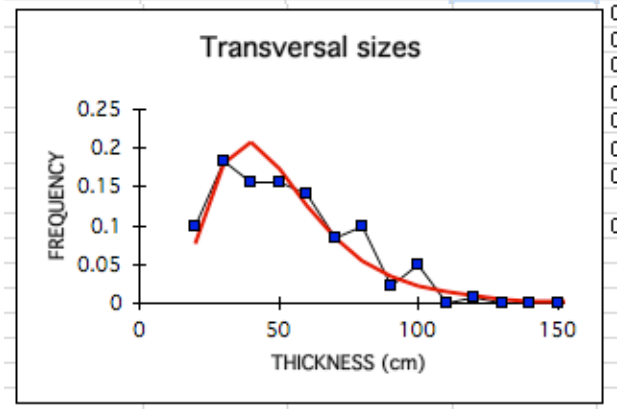

MEAN SIZE=	51.7
ALPHA=	3.846
BETA^2=	0.208

Both of the above distributions pass the Kolmogorov-Smirnov test for lognormal shape (the red curves) at the > 10% level, the most significant level in the tables.

Bove, D., Eberl, D., McCarty, D., and Meeker, G. (2002) Characterization and modeling of illite crystal particles and growth mechanisms in a zoned hydrothermal deposit, Lake City, Colorado. American Mineralogist, 87, 1546-1556.

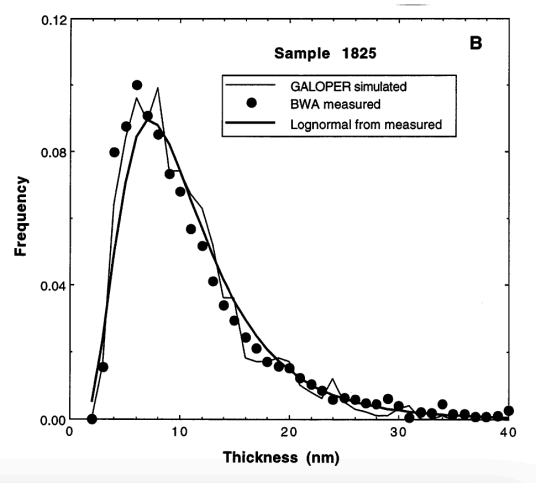

Figure 5b. Lognormal shape for illite crystal thicknesses from Red Mountain, Colorado. Alpha = 2.24, and beta^2 = 0.32.

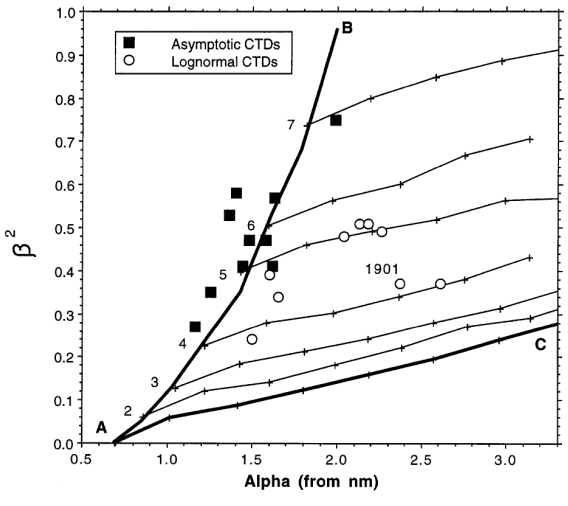

FIGURE 6. Alpha-β^2 diagram showing these parameters for illite crystallite thickness distributions having the two basic shapes. See text for explanation.

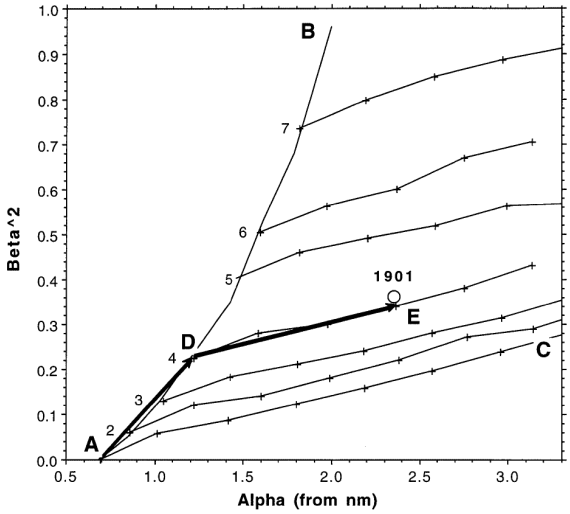

FIGURE 7. Alpha-β^2 digram showing the unique reaction path (A-D-E) that simulates the shape of the crystallite thickness distribution for sample 1901.

De Yoreo, J.J., Gilbert, P.U.P.A., Sommerdijk, N.A.J.M., Penn, R.L., Whitelam, S., Joester, D., Zhang, H., Rimer, J.D., Navrotsky, A., Banfield, J.F., Wallace, A.F., Michel, F.M., Meldrum, F.C., Cölfen, H., and Dove, P.M. (2015) Crystallization by particle attachment in synthetic, biogenic, and geologic environments. Science, 349, print extended abstract at pg. 498, online at aaa6760 DOI: 10.1126/science.aaa6760.

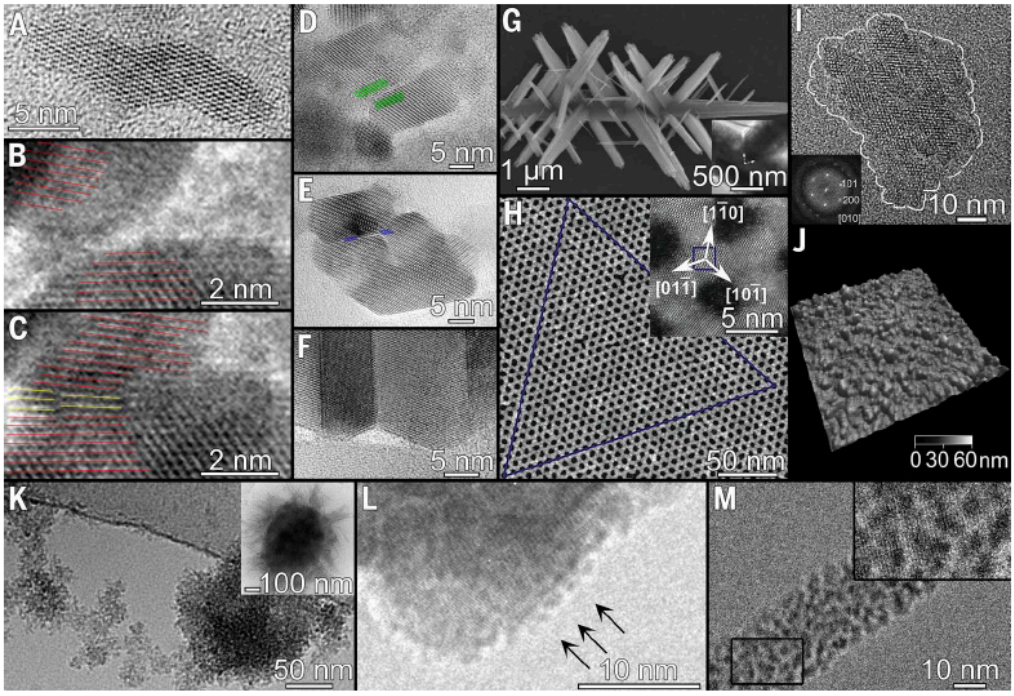

Fig. 2. Examples of inorganic crystals formed by CPA. (**A**) Nanoparticles of anatase (TiO_2) with perfect alignment after apparent attachment event with the *c* axis oriented along the long dimension of the aggregate (*116*). (**B** and **C**) Sequential in situ images showing oriented attachment of ferrihydrite with creation of an edge dislocation (yellow lines) and resulting tilt of lattice planes above and below the edge dislocation (red lines) (*27*, *30*). (**D** to **F**) TiO_2 nanocrystals showing defects incorporated through CPA, including (D) low-angle tilt boundaries, (E) screw dislocations, and (F) twin planes. In (E), the variations in contrast and slight shift in lattice fringe clarity and alignment indicate incorporation of defects. The blue lines highlight the orientation and shift in lattice fringe alignment to either side of the region that contains the dislocations; the bright-dark contrast is consistent with a dislocation having a screw component. (**G**) Branched nanowire of rutile (TiO_2), where each branch occurs on a set of twin boundaries (inset) (*60*). (**H**) Single-crystal honeycomb superlattice formed through oriented attachment of PbSe nanocrystals in an octahedral symmetry. The equilateral triangle shows the long-range ordering of the structure, and the inset shows the relationship of the crystalline axes with the superlattice pattern (*39*) (**I**) Cryo-TEM micrograph of a single zeolite nanoparticle (*117*). (**J**) Atomic force micrograph of a zeolite surface showing that its growth proceeds by attachment of silica nanoparticles (*28*). (**K**) Calcium phosphate prenucleation complexes aggregating to form amorphous calcium phosphate nanoparticles. (Inset) Amorphous calcium phosphate nanoparticle is replaced by outgrowths of calcium-deficient octacalcium phosphate (*5*). (**L**) Magnetite crystal growing through the accretion of disordered ferrihydrite-like nanoparticles (*57*). (**M**) Goethite mesocrystal formed by the assembly of nanocrystals shows lattice fringes that correspond to (021) planes (*62*).

Eberl, D. (2022) On the formation of Martian blueberries. American Mineralogist, 107, 153-155.

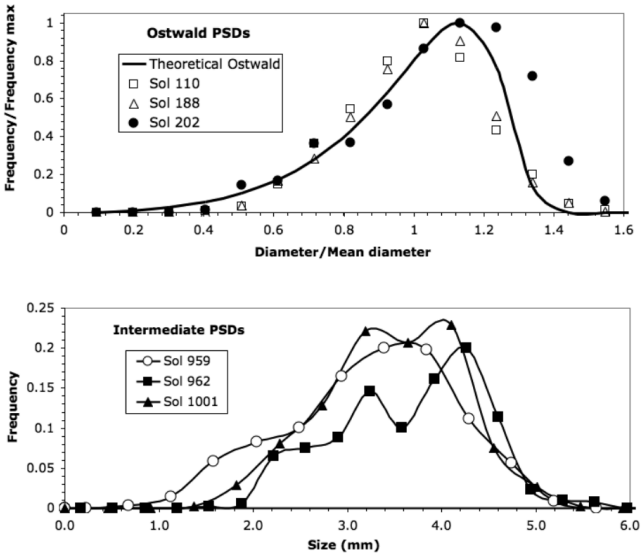

FIGURE 2. Changes in the shapes of particle size distributions as the rover neared Endurance Crater rim (upper) and Victoria Crater rim (lower), showing a change from the universal steady-state Ostwald-shaped reduced PSDs (upper) to transitional PSDs (lower). The original PSD data comes from Royer et al. (2008).

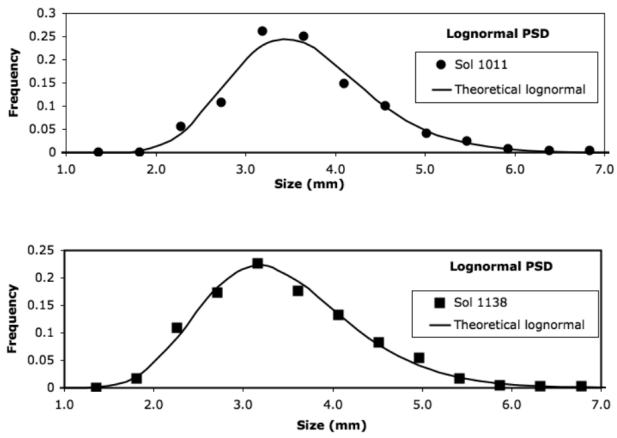

FIGURE 3. The two best examples of lognormal PSDs from Victoria Crater rim. The other four samples in this data set skew to the right, and pass the Kolmogorov-Smirnov statistical test for log normality: sol 1124 from 1 to 5%, sol 1071 from 5 to 10%, and sols 1113 and 1139 (and the two sols shown above) to the >10% level of confidence, the highest level in the tables. The original PSD data comes from Royer et al. (2008).

Eberl, D. (2004) Quantitative mineralogy of the Yukon River system: Changes with reach and season, and determining sediment provenance. American Mineralogist, 89, 1784-1794.

Figure 18B

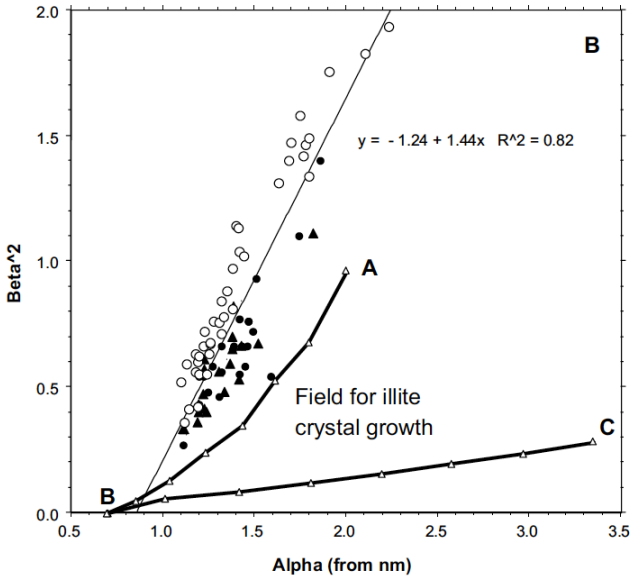

(see text). (**b**) Plot of α and β^2 values for crystallite size distributions for illites found in suspended sediments (open circles), Yukon River bed sediments (filled circles), and tributary bed sediments (filled triangles).

Eberl, D., Drits, V., and Srodon, J. (1998) Deducing crystal growth mechanisms for minerals from the shapes of crystal size distributions. American Journal of Science, 298, 499–533.

TABLE 2

Summary of crystal growth mechanisms and their characteristics

System	Growth Mechanism	CSD Shape	Comments
Open	Nucleation and growth with constant or accelerating nucleation rate.	Asymptotic.	β^2 increases exponentially with increase in α.
	Nucleation and growth with decaying nucleation rate.	Lognormal.	β^2 increases linearly with increase in α.
	Surface-controlled growth.	Lognormal.	β^2 increases linearly with increase in α.
	Supply-controlled growth.	Preserves shape of previous CSD.	β^2 remains constant with increase in α; therefore, steady-state reduced profiles.
Closed	Ostwald ripening (supply-controlled).	CSD becomes more symmetrical with increasing percentage of ripening, becomes negatively skewed, and eventually approaches universal steady-state reduced profile.	Distribution maximum moves to the right of theoretical lognormal curve. Generally, β^2 decreases with increase in α. Universal steady-state profile may not be reached.
	Random ripening (supply-controlled). Also termed non-Ostwald or kinetic ripening.	Preserves shape of previous CSD.	A large amount of material passes through solution for a small increase in mean size. β^2 remains constant with increase in α; therefore steady-state reduced profiles.
	Agglomeration.	Can be pseudo-lognormal or multimodal, or have other shapes.	Very little material need pass through solution for a large increase in mean size. If most of the crystals are involved, β^2 may decrease; otherwise it may increase.

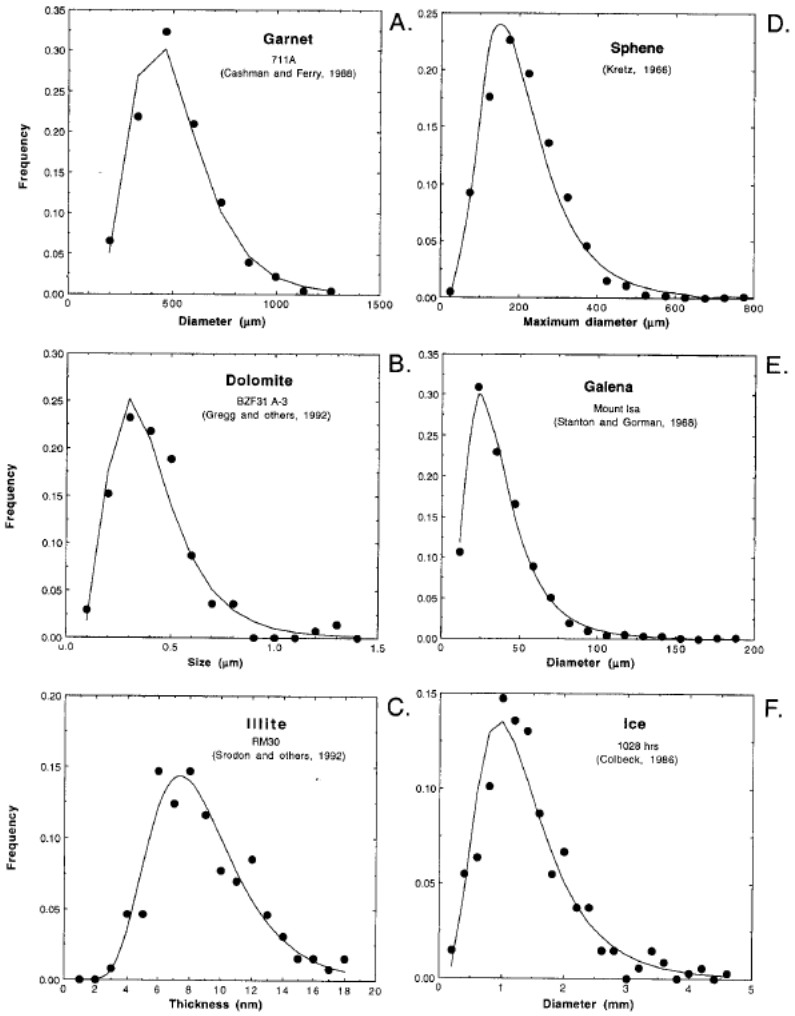

Fig. 1. Particle size data from the literature (points), with superimposed theoretical lognormal curves calculated from these data (solid lines).

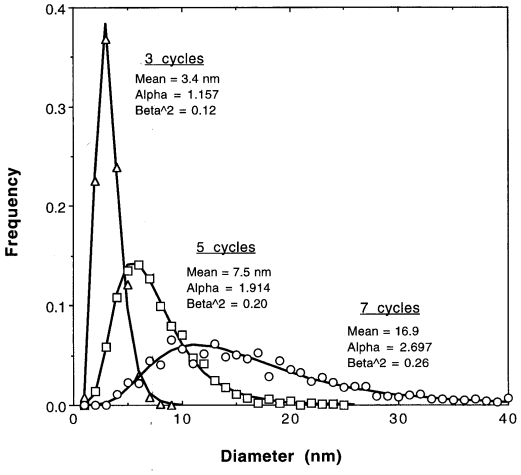

Fig. 2. GALOPER-calculated CSDs (symbols) for surface-controlled open system growth, using 3, 5, and 7 calculation cycles (eq 5) and an initial crystal diameter of 1 nm, compared with theoretical lognormal curves calculated from these data (solid lines).

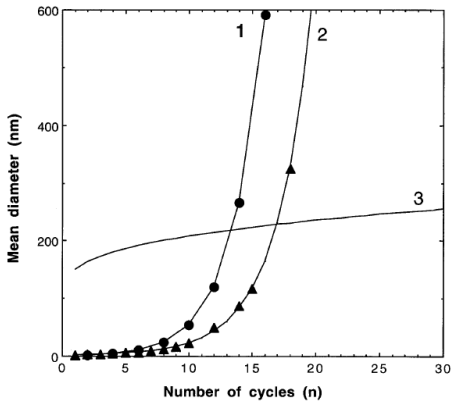

Fig. 3. Plots of rate equations (solid curves) for: (1) surface-controlled open system growth (eq 6 in text) starting with 2 nm crystals; (2) constant-rate nucleation and growth (eq 7 in text) starting with 2 nm crystals; and (3) supply-controlled growth (eq 9 in text) starting with a mean size of 100 nm and using k = 50. Epsilon was allowed to vary between 0 and 1 for all calculations (that is, ε = 0.5). The symbols represent GALOPER calculations for the corresponding growth mechanisms.

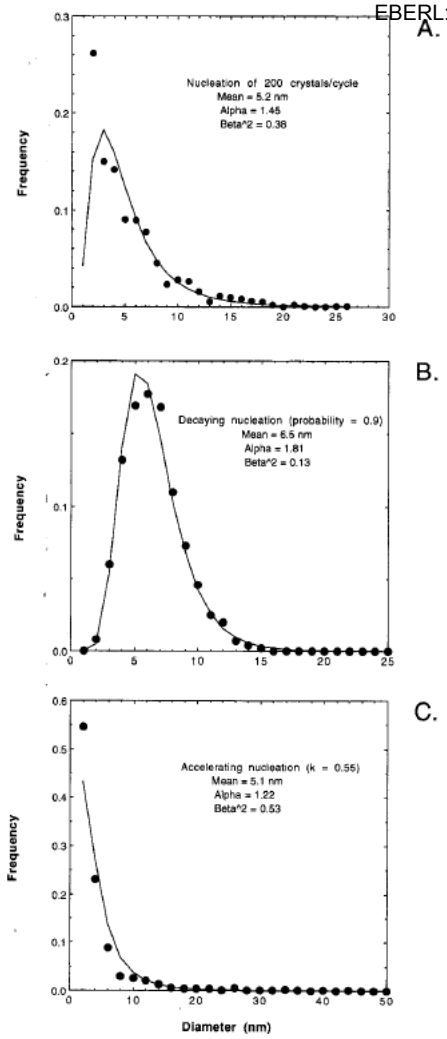

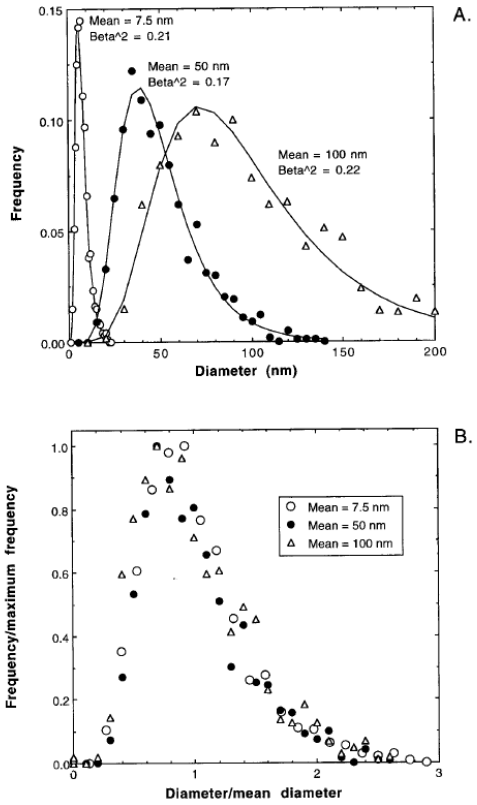

Fig. 6. GALOPER-calculated CSDs for supply-controlled open system overgrowth starting with a lognormal distribution. (A) = overgrowth starting with a lognormal CSD having a mean size of 7.5 nm; (B) = Steady-state reduced plot of CSDs in (A).

Fig. 4. GALOPER-calculated CSDs (points) for the continuous nucleation and growth mechanism assuming nucleation having: (A) a constant rate; (B) a decaying rate; and, (C) an accelerating rate. Critical nucleus size = 2.0 nm. The solid lines are lognormal fits to the data.

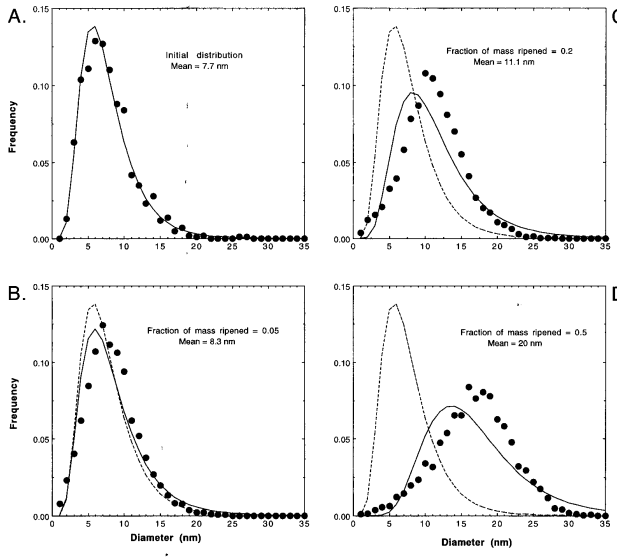

Fig. 8. GALOPER-calculated CSDs modified by Ostwald ripening. (A) = initial distribution; (B) = 5 percent of the initial mass has passed through solution once; (C) = 20 percent through solution; (D) = 50 percent through solution. The solid curves are theoretical lognormal curves calculated from the ripened CSDs (solid circles). The dashed curves are the shape of the original lognormal CSD in (A).

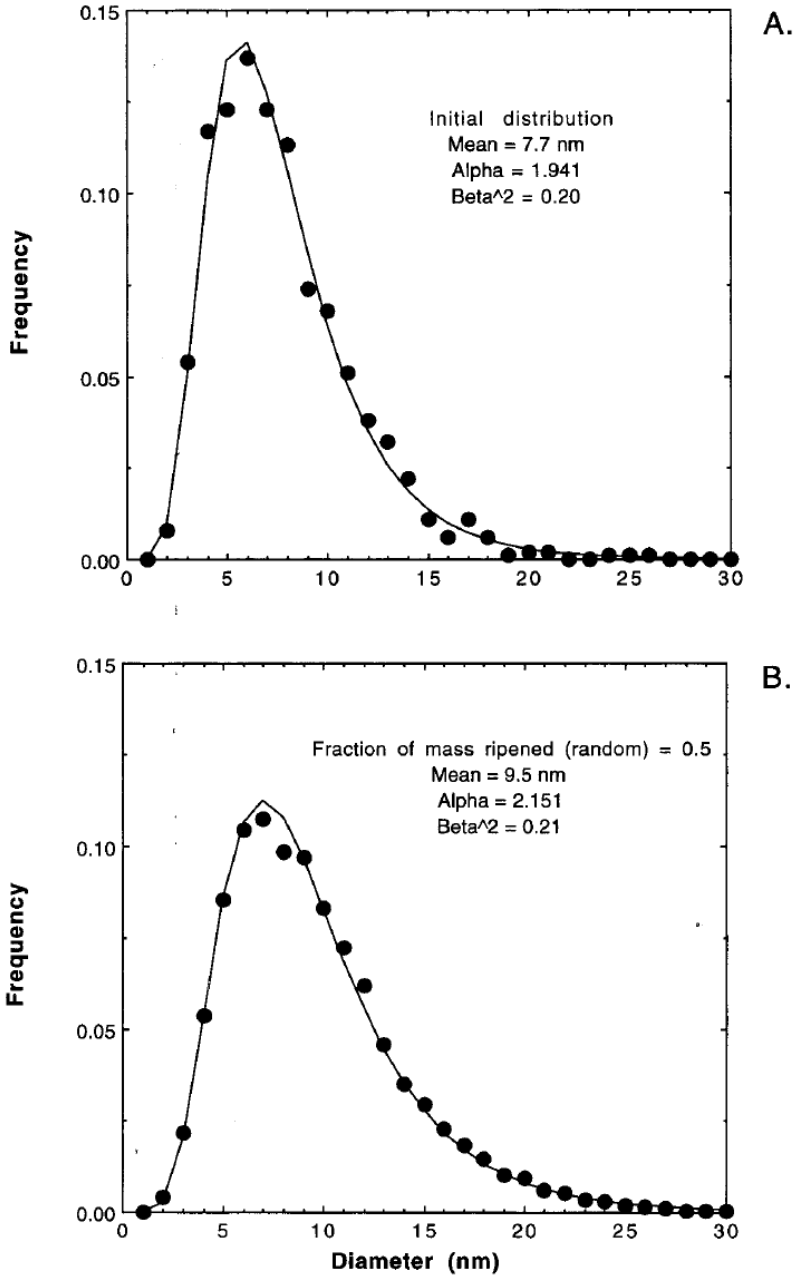

Fig. 11. GALOPER-calculated CSDs for random ripening. (A) = initial distribution; (B) = 50 percent of initial mass has passed through solution by supply-controlled random ripening. The solid circles are the calculated CSDs, and the solid lines are the theoretical lognormal curves.

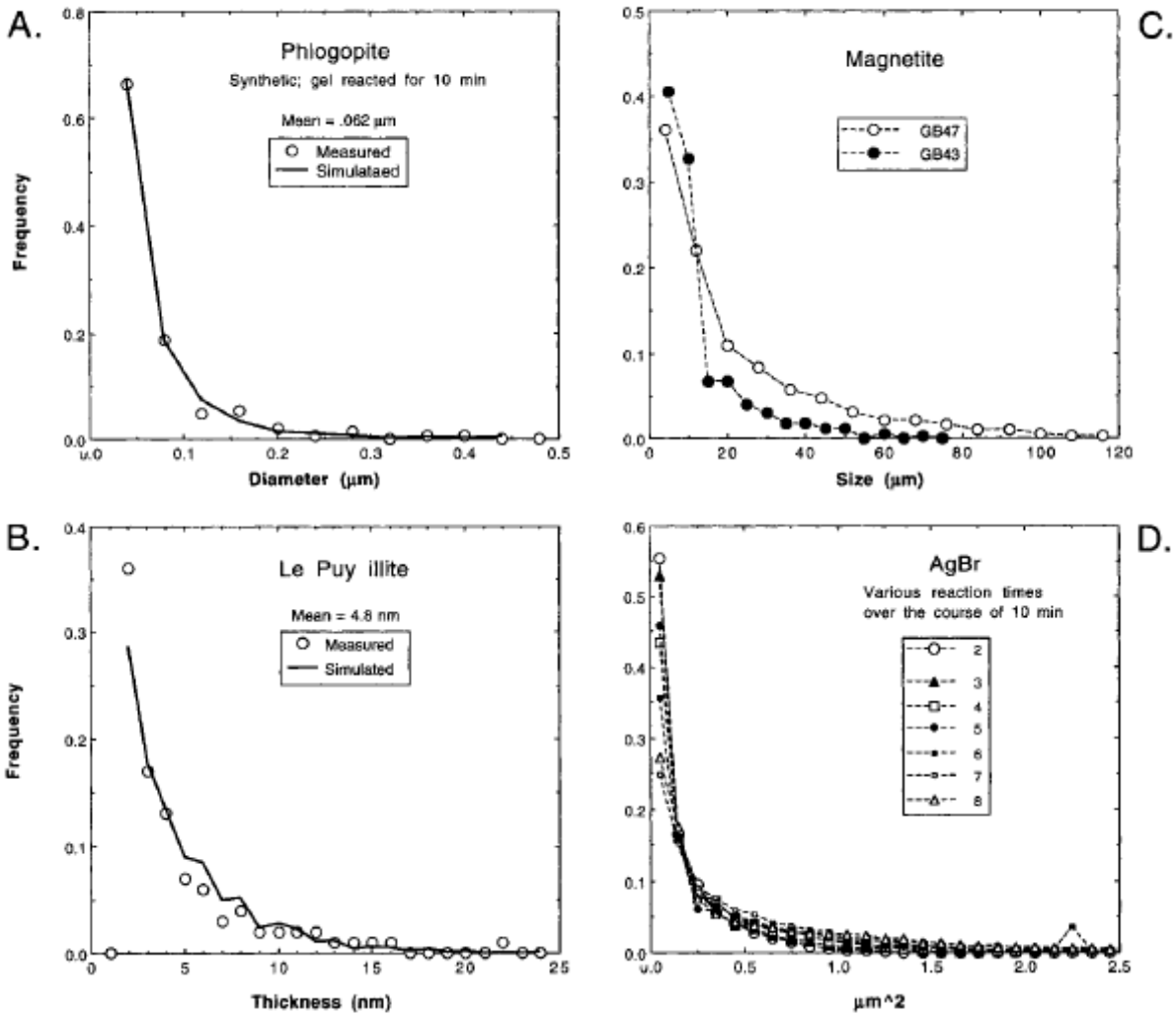

Fig. 13. Measured asymptotic-type CSDs for minerals, and GALOPER simulations. Shapes of CSDs are attributed to nucleation and growth with constant nucleation rate. (A) Phlogopite mean a-b diameters from Baronnet (1974 and personal communication), with GALOPER simulation (solid curve); (B) Le Puy illite thickness distribution, measured by the Bertaut-Warren-Averbach XRD method (Drits and others, 1998; Eberl and others, 1998), and GALOPER simulation (solid curve); (C) Magnetite from Cashman and Ferry (1988); AgBr data from Loveland and Trivelli (1947; L-1 precipitation, their fig. 7).

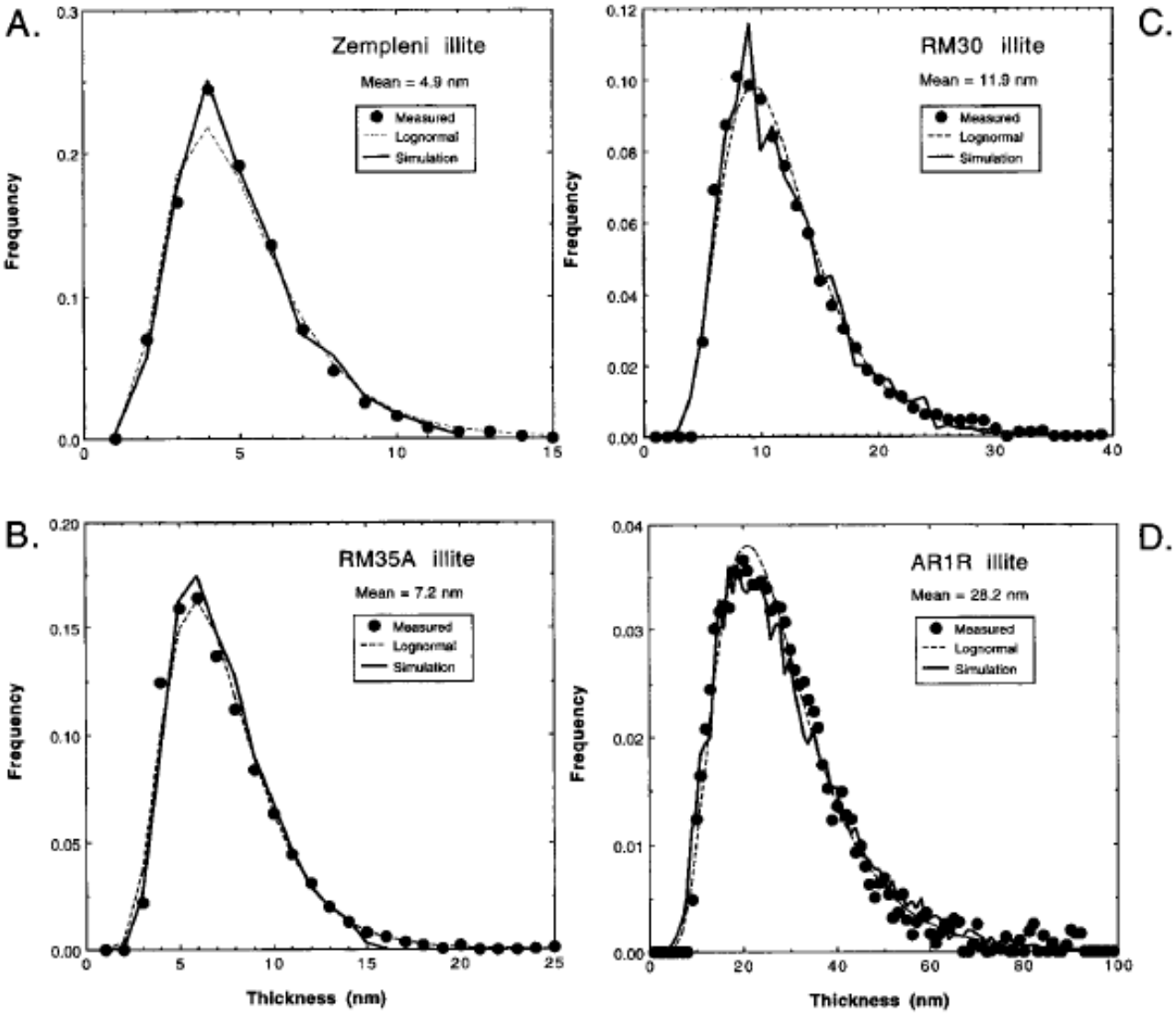

Fig. 15. Fundamental illite crystal thickness distributions for hydrothermal illites, measured by the authors by X-ray diffraction (Drits and others, 1998; Eberl and others, 1998). Points = measured distributions; dashed lines = lognormal curves calculated from the measurements; solid lines = GALOPER simulations. For information on the samples: (A) (Viczián, 1997); (B, C, and D) (Eberl and others, 1987).

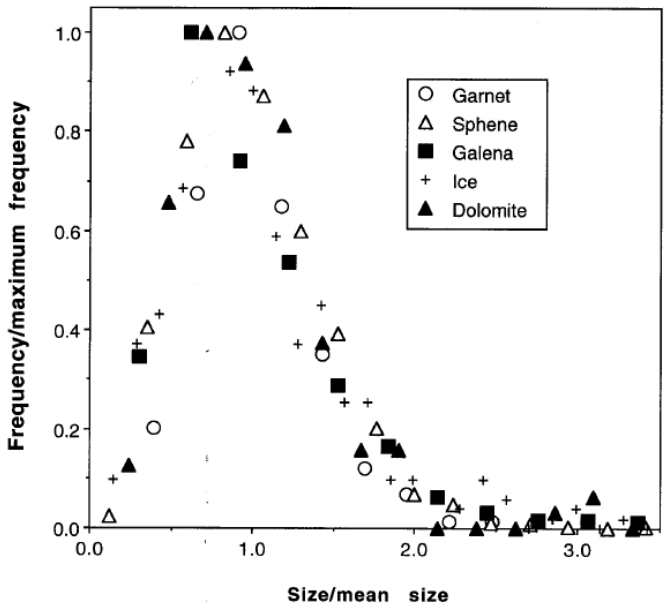

Fig. 16. Reduced CSDs calculated for minerals in figure 1, demonstrating steady-state shape.

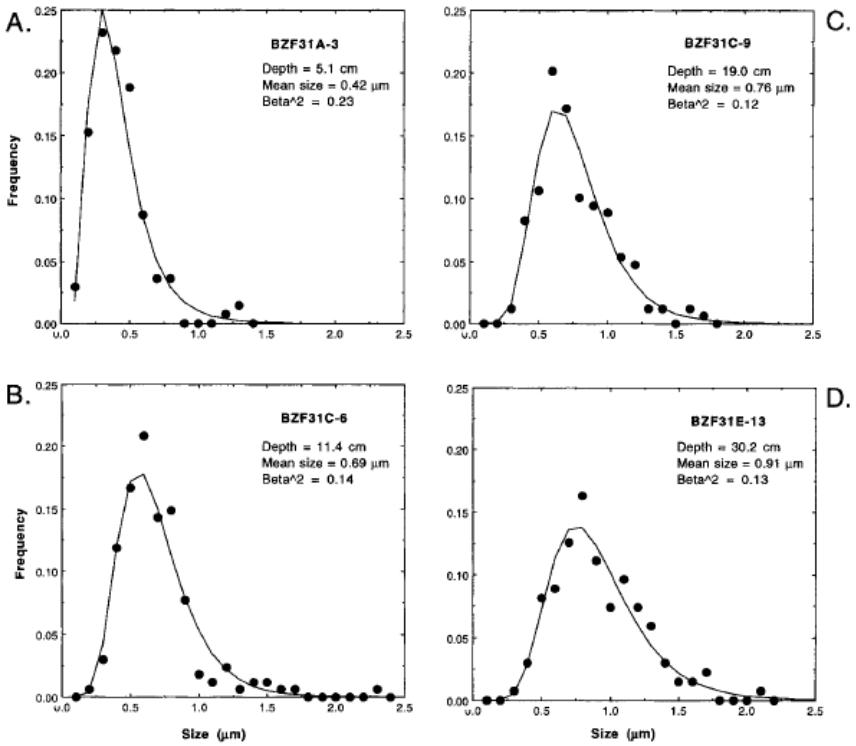

Fig. 17. Measured CSDs (symbols) compared with theoretical lognormal curves (solid lines) for dolomite CSDs collected at various depths from crusts from the bottom of Ambergris Cay, Belize (Gregg and others, 1992, and personal communication).

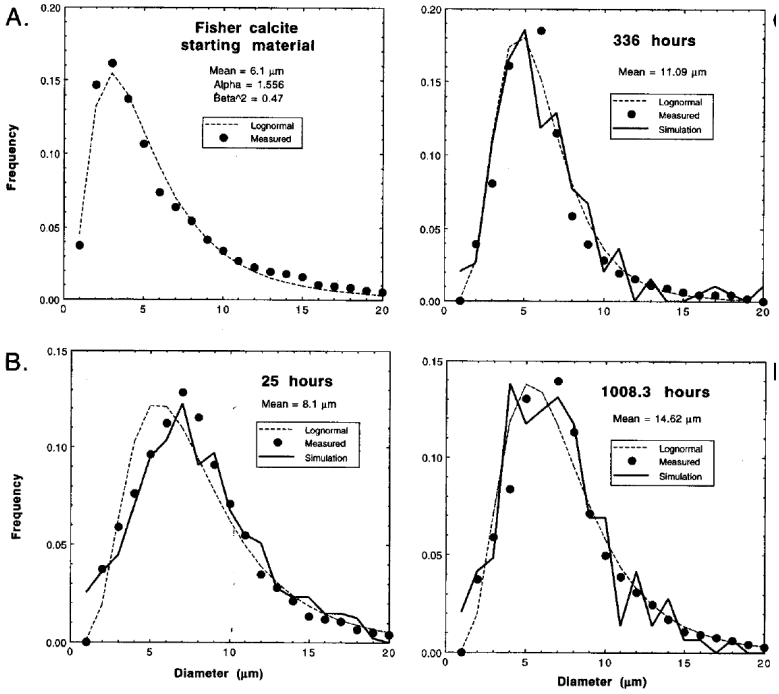

Fig. 18. CSDs (from figs. 44 and 45 in Chai, ms) from calcite ripening experiments compared with theoretical lognormal (dashed curves) and GALOPER simulations (solid curves). The initial Fisher calcite was ripened at 500°C and 2 kb for different lengths of time.

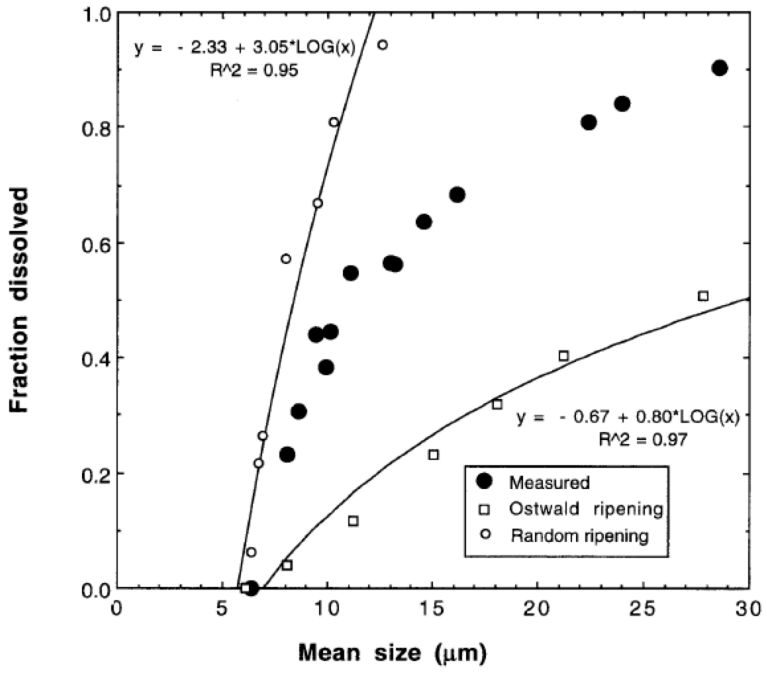

Fig. 19. Fraction dissolved (from oxygen isotope measurements) versus increase in mean crystal size for calcite ripening experiments, compared with theoretical, GALOPER-calculated curves for random ripening (upper curve) and Ostwald ripening (lower curve). Data from table 5 in Chai, ms).

Equation 8:

Supply-controlled growth in the open system.–One can imagine an open system in which the rate of crystal growth is controlled by the rate of nutrient supply rather than by the rate at which the crystal surface can grow in an infinite reservoir of nutrients. For example, the supply may be slowed by diffusion or by the rate of dissolution of an unstable phase that is a nutrient source, or crystals may grow so large that supply can not keep up with the exponentially increasing demand for nutrients required by LPE growth. This situation is simulated in GALOPER by specifying the total increase in volume that 1001 crystals are permitted ($\Sigma\Delta V_a$) during each cycle of eq (5). The crystals first are allowed to grow freely during a calculation cycle according to eq (5). Next the growth volume for that cycle for each crystal is calculated ($\Delta V_{j,LPE}$), and the growth volumes for all crystals are summed ($\Sigma\Delta V_{j,LPE}$). The unconstrained growth volume for each crystal then is reduced proportionately by the ratio of allowed volume to unconstrained growth volume:

$$\Delta V_j = (\Delta V_{j,LPE})\frac{\Sigma\Delta V_a}{\Sigma\Delta V_{j,LPE}}. \quad (8)$$

The corrected growth volume for each crystal (ΔV_j) is added to the previous volume of the crystal, and a new diameter for each crystal for that growth cycle is then calculated from the equation for the volume of a sphere. The calculation is repeated for each growth cycle. Therefore, during this type of growth the LPE is still the growth law, but growth is limited proportionately by supply.

Equation 10:

2. For diffusion-controlled ripening, the instantaneous rate at which a crystal changes size is given by:

$$\frac{dr}{dt} = \frac{K}{r}\left(\frac{1}{r^*} - \frac{1}{r}\right), \quad (10)$$

where r = the crystal radius, t = time (or calculation cycles), r* = the critical radius, which is equal to the mean radius ($\bar{r}$), and K is a constant (see app. 2).

Equation A20:

A remarkable feature of surface- and supply-controlled Ostwald ripening is the evolution of the crystal size distribution with the passage of time. It was shown by Lifshitz and Slyozov (1961) and Wagner (1961) that at large time this distribution can be approximated by certain universal functions that develop irrespective of the initial CSD. For example, in the case of supply-controlled crystal growth this function has the form:

$$f(r, t) = \text{Const}\frac{(t^{-4/3})u^2}{(3 - 2u)^{11/3}(3 + u)^{7/3}}\exp\left(\frac{3}{2u - 3}\right), \quad (A20)$$

where $u = r/\bar{r} = r/r^*$. As can be seen in figure 9A, normalized f(r, t) has an asymptotic profile with two characteristic features: (A) this function is equal or very close to zero at $u > 3/2$ or $r > (3/2)\bar{r}$; (B) it has a left-hand skewed distribution of crystal sizes.

Eberl, D., Kile, D., and Drits, V. (2002a) On geological interpretations of crystal size distributions: Constant vs. proportionate growth. American Mineralogist, 87, 1235–1241.

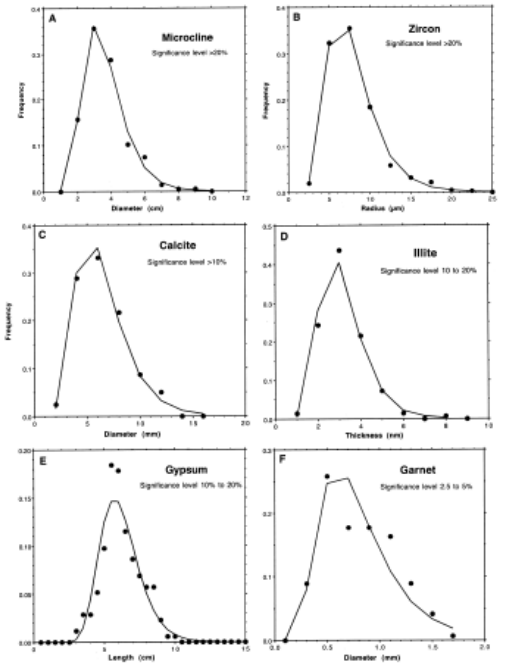

FIGURE 1. CSDs (solid circles) and lognormal fits (lines) with significance levels for chi-square test between the two. (A) Microcline, 1989 (Kile and Eberl 1999); (B) Zircon B, L total (Nemchin et al. 2001); (C) Calcite, SE Colorado (Kile et al. 2000); (D) Illite, Zamplemi (Srodoń et al. 2000); (E) Gypsum from Jet, Oklahoma (this paper); (F) Garnet, Spaciman 2 (Krotz 1966). Only the zircon CSD measurement (Fig. 1B) possibly is subject to stereological problems because it was measured from thin section.

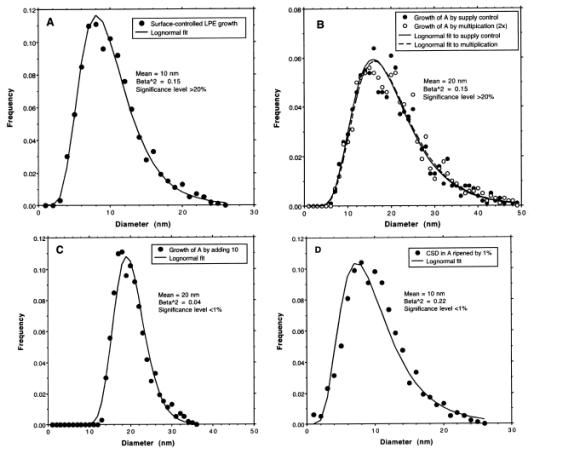

FIGURE 2. The effect of growth mechanisms on the shape of a lognormal CSD. (A) Initial lognormal CSD (circles), simulated in GALOPER by LPE growth (Eq. 3; GALOPER option 5), with lognormal fit (line). (B) CSD in (A) is doubled in size by supply controlled growth (solid circles; GALOPER option 6) and by multiplication of the crystal sizes by 2 (open circles). (C) CSD in (A) is doubled in size by adding 10 nm to each crystal size. (D) CSD in (A) is Ostwald ripened (GALOPER closed system option 1), allowing 1% of the crystal mass to pass through solution.

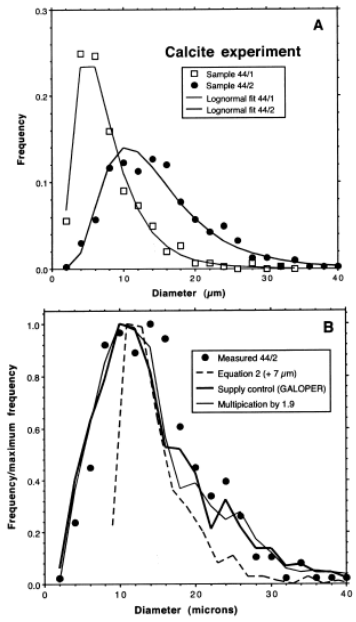

FIGURE 3. CSDs measured (Kile et al. 2000) and calculated for calcite growth experiments. (A) Initial, measured CSD (CCNG-44/1; squares) and final, measured CSD (CCNG-44/2; circles) with lognormal fits (solid lines). The two calcites were taken from the same solution after different reaction times. (B) The final, normalized, measured CSD (CCNG-44/2; circles) modeled from the initial CSD (CCNG-44/1) by Equation 2 (broken line), by supply controlled modification of Equation 3 using the GALOPER program (thick solid line), and by multiplying by a constant (thin solid line).

Ivanov, V.K., Fedorov, P.P., Baranchikov, A.Y., and Osiko, V.V. (2014) Oriented attachment of particles: 100 years of investigations of non-classical crystal growth. Russian Chemical Reviews 83, 1204-1222.

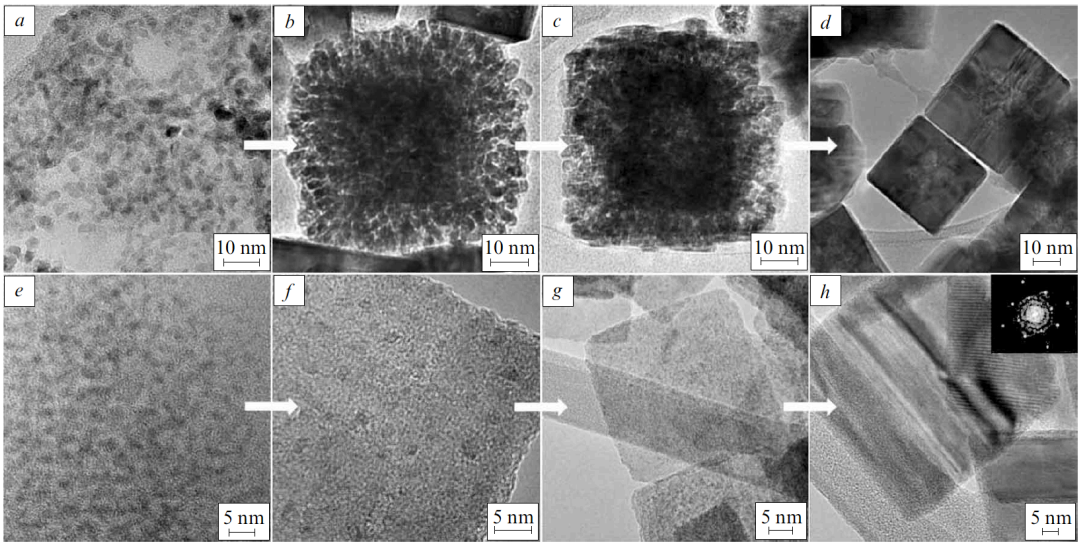

Figure 12. TEM images reflecting the sequence of stages in the oriented attachment of nanocrystals.[140]
(*a*) Original FeS_2 crystals, (*b*) agglomeration of crystallites, (*c*) attachment of crystallites, (*d*) recrystallization to form cubic single crystals, (*e*–*h*) formation of thin FeS_2 plates as a result of attachment and recrystallization processes.

Kile, D. and Eberl, D. (1999) Crystal growth mechanisms in miarolitic cavities of the Lake George ring and vicinity, Colorado. American Mineralogist, 84, 718-724.

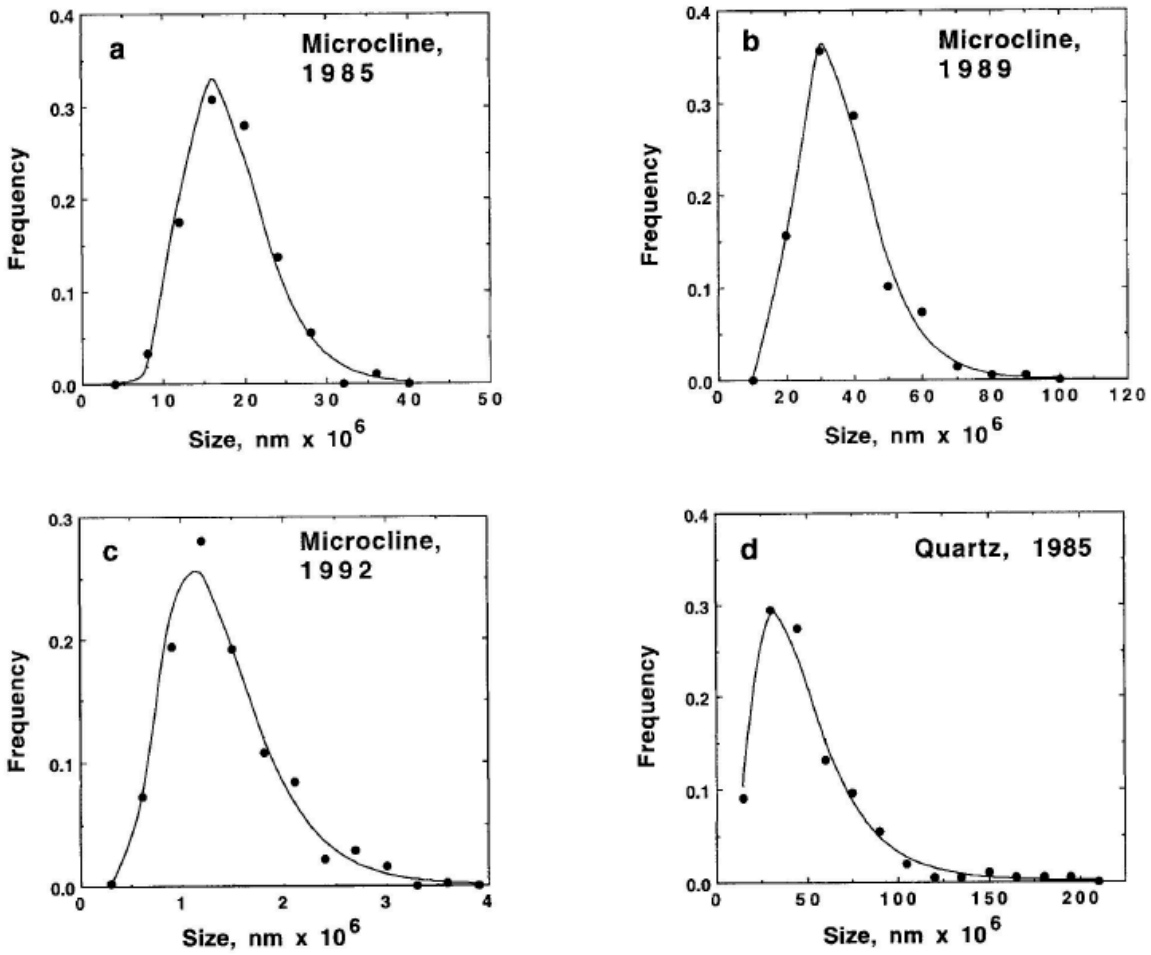

FIGURE 2. Representative plots showing CSDs superimposed on the theoretical lognormal curves (solid lines): (a) microcline, LGR, 1985; (b) microcline, LGR, 1989; (c) microcline, north of LGR, 1992; and (d) quartz, LGR, 1985.

Kile, D. and Eberl, D. (2003) On the origin of size-dependent and size-independent crystal growth: Influence of advection and diffusion. American Mineralogist, 88, 1514-1521.

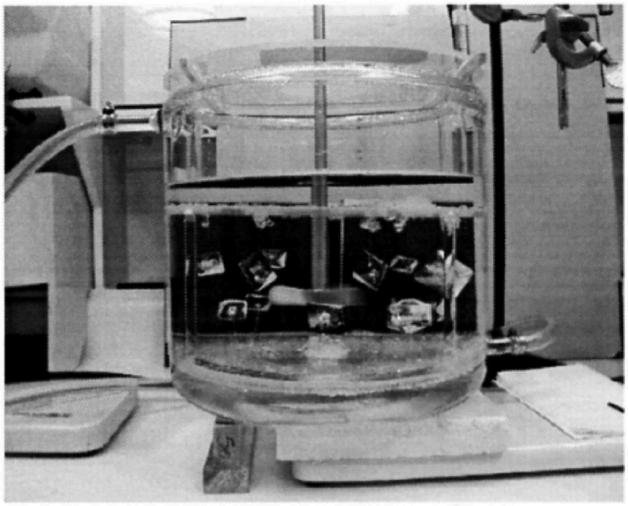

FIGURE 1. Water-jacketed crystallization vessel with variable-speed stirrer for alum experiments.

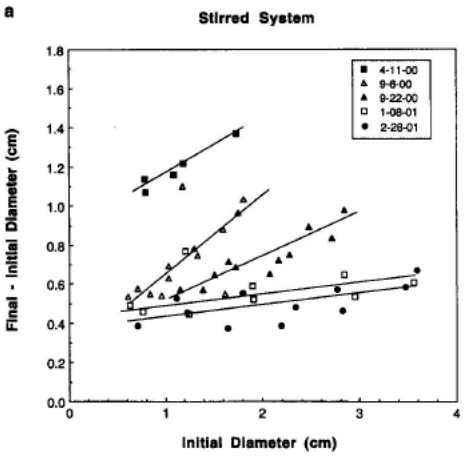

FIGURE 2. Growth rate as a function of initial crystal size measured for (a) stirred and (b) unstirred systems for alum crystals.

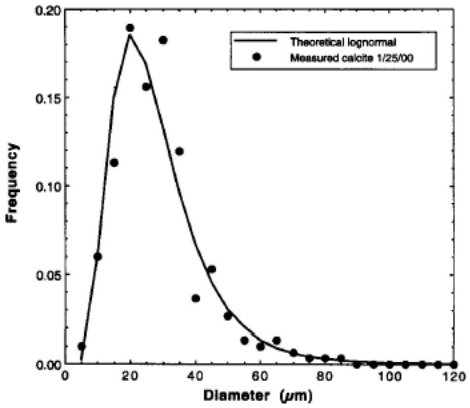

FIGURE 3. CSD for calcite formed in a non-stirred system, with theoretical lognormal curve.

Figure 4C

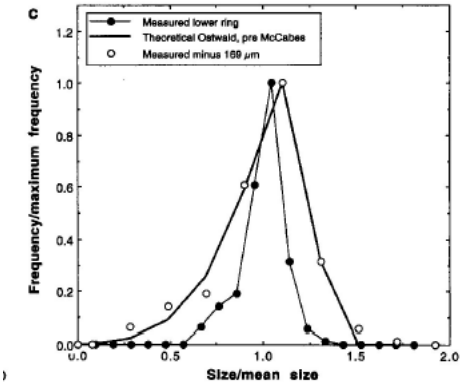

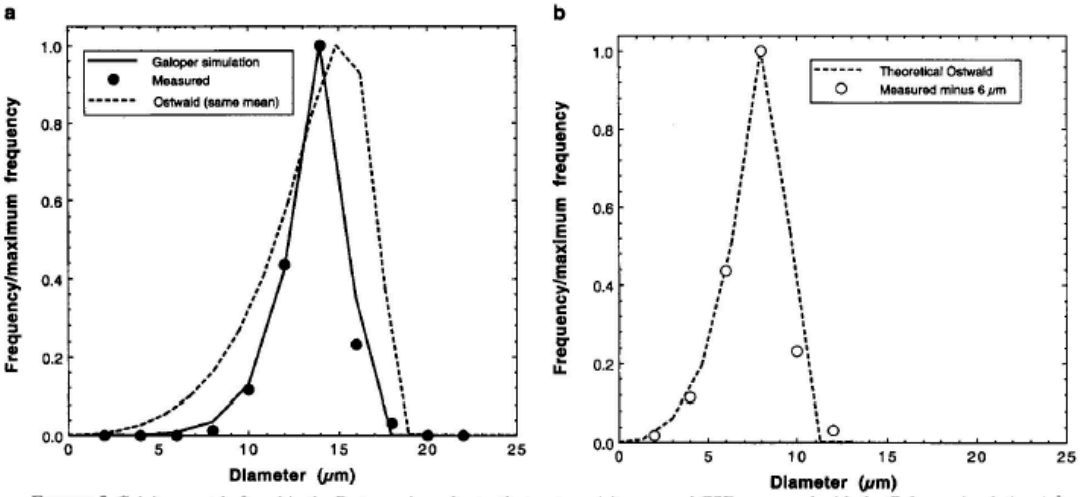

FIGURE 5. Calcite crystals found in the Proterozoic molar tooth structure: (a) measured CSD compared with the Galoper simulation ($\chi^2 >$ 20%) and the theoretical CSD expected for Ostwald ripening; (b) measured CSD with constant growth stage subtracted from the crystal sizes compared with the theoretical Ostwald curve.

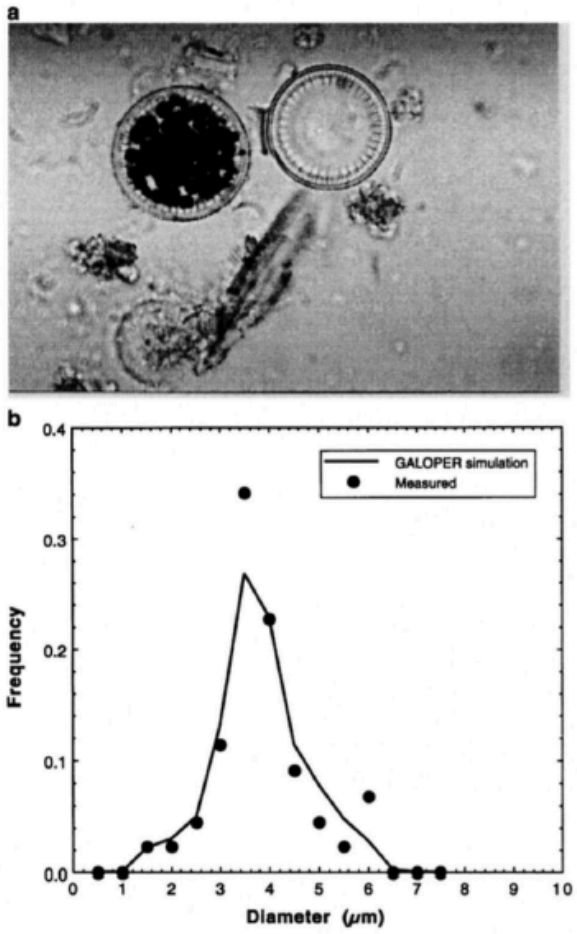

FIGURE 6. Greigite (?) from Pyramid Lake, Nevada: (a) photomicrograph of crystals found within diatom tests, and (b) CSD measured for crystals compared with a Galoper simulation (χ^2 significance >20%).

Kile, D., Eberl, D., Hoch, A., and Reddy, M. (2000) An assessment of calcite crystal growth mechanisms base on crystal size distributions. Geochimica et Cosmochimica Acta, 64, 2937-2950.

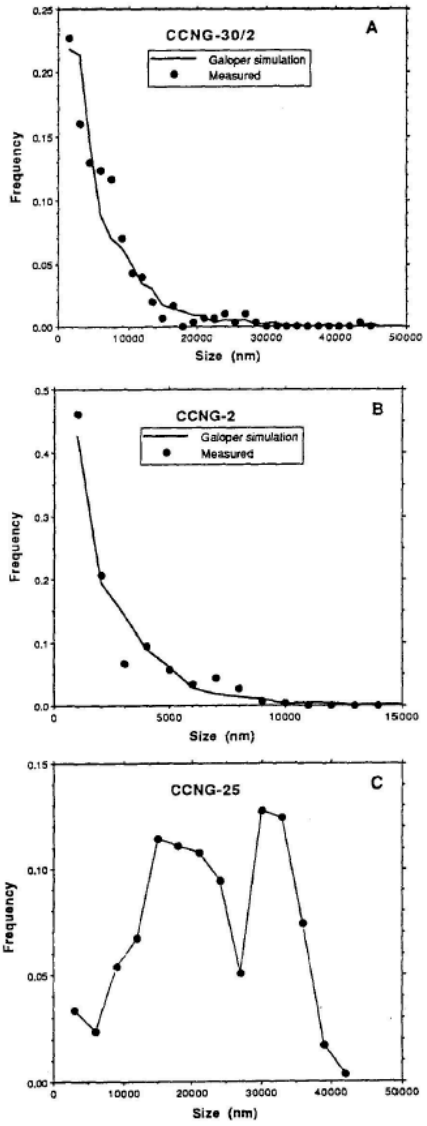

Fig. 2. (A) Characteristic asymptotic CSD for sample CCNG-30/2. The Galoper simulation used a critical nucleus size of 3 nm (read from Fig. 10, using $\Omega = 20$ from Table 1) with 143 crystals nucleating per calculation cycle, followed by supply-controlled growth to the correct mean size; level of significance for χ^2 comparison between simulated and measured CSDs = 2.5 to 5%. (B) Characteristic asymptotic CSD for sample CCNG-2. CSD simulated as in A, with significance level = 1 to 5%. (C) Bimodal CSD resulting from sequential addition of $CaCl_2$ and KOH for sample CCNG-25.

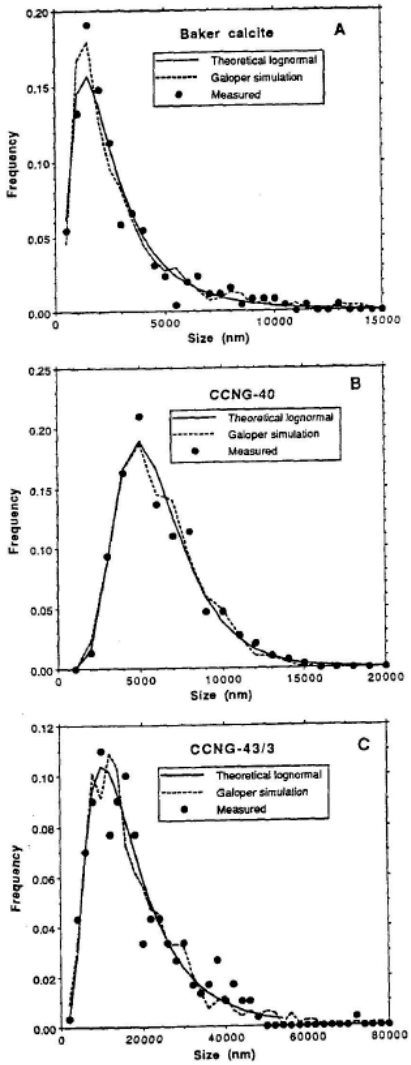

Fig. 3. (A) Plot of size vs. frequency showing lognormal CSD for Baker calcite. Galoper simulation used a critical nucleus size of 3 nm and a probability for nucleation of 0.6, followed by supply-controlled growth; significance level for χ^2 comparison between simulation and measurements = 10 to 20%. (B) Plot of size vs. frequency for a typical lognormal profile of synthetically grown calcite (CCNG-40). Galoper simulation used a critical nucleus size of 2.5 nm (Table 1 and Fig. 10) and a probability for nucleation of 0.85, followed by supply-controlled growth; significance level > 20%. (C) Plot of size vs. frequency for a typical lognormal profile of synthetically grown calcite (CCNG-43/3). Galoper simulation used a critical nucleus size of 3 nm (Table 1 and Fig. 10), and a probability for nucleation of 0.60; significance level > 20%.

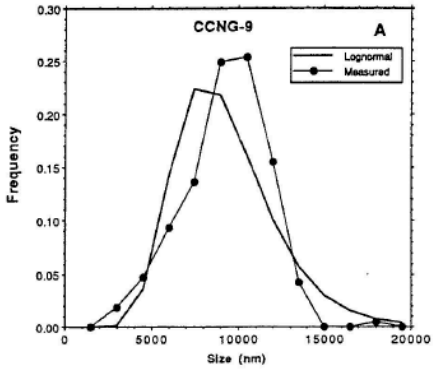

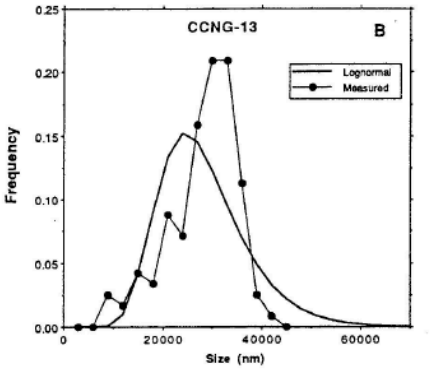

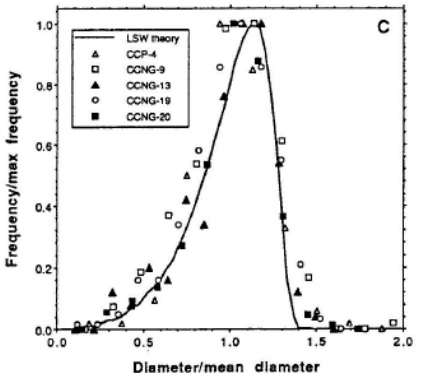

Fig. 4. (A) Negatively skewed CSD characteristic of Ostwald ripening (CCNG-9). (B) Negatively skewed CSD characteristic of Ostwald ripening (CCNG-13). (C) Reduced plot showing ripened samples with the theoretical, universal, steady-state curve expected for diffusion-controlled Ostwald ripening according to the LSW theory, with ripened samples.

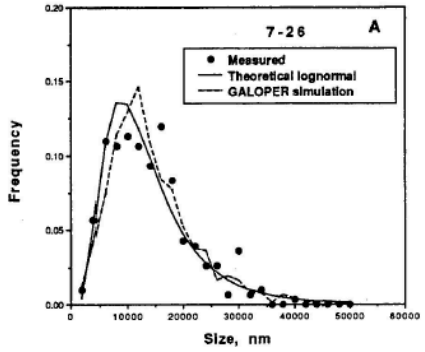

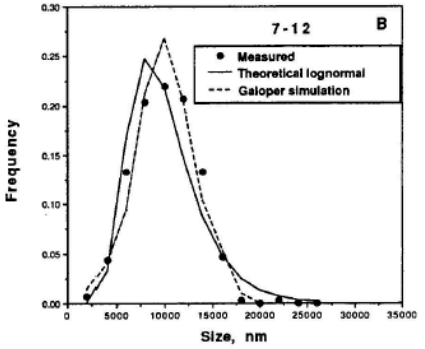

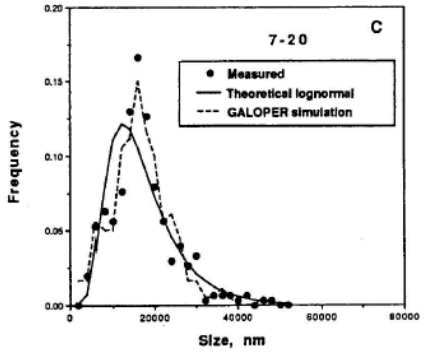

Fig. 5. (A) Transitional CSD (sample 7-26) with a shape that is intermediate between lognormal and Ostwald curves. Starting Ω = 28.2. χ^2 significance between experimental data and Galoper simulation = 5 to 10%. (B) Transitional CSD (sample 7-12) with a shape that is intermediate between lognormal and Ostwald curves. Starting Ω = 53.7. χ^2 significance between experimental data and Galoper simulation = 10 to 20%. (C). Transitional CSD (sample 7-20) with a shape that is intermediate between lognormal and Ostwald curves. Starting Ω = 69.2. χ^2 significance between experimental data and Galoper simulation = > 20%.

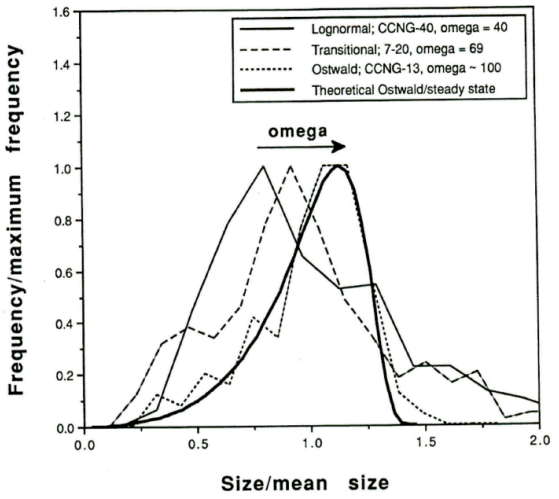

Fig. 6. Reduced plot of lognormal, transitional, and Ostwald CSDs showing a progressive shift with increasing Ω toward the theoretical Ostwald steady-state curve.

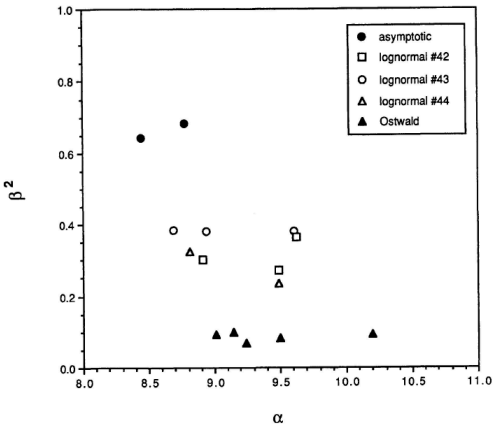

Fig. 7. Plot of size variance (β^2) vs. natural log mean size (α) for synthetic calcite.

A.

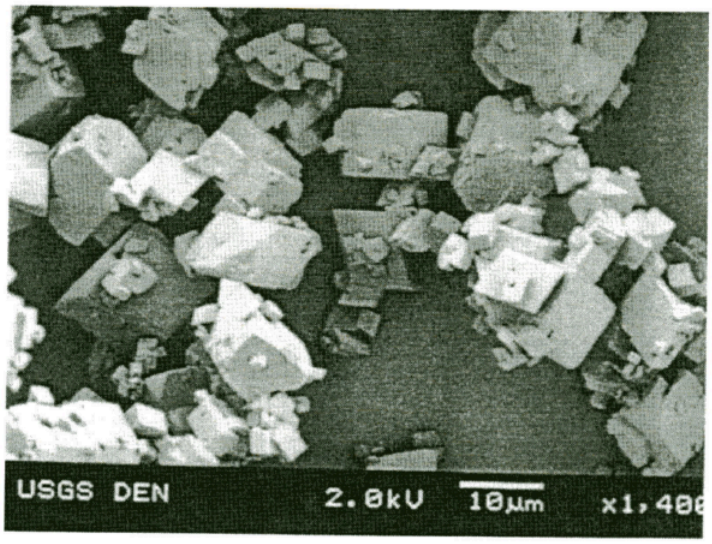

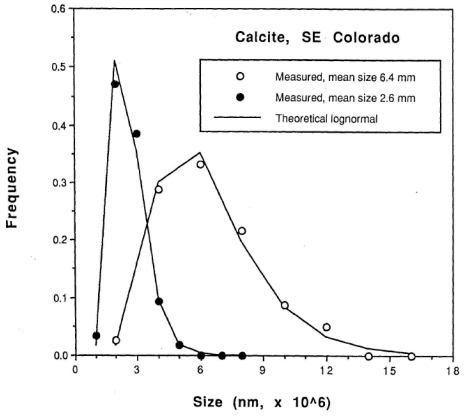

Fig. 9. Lognormal size distributions for two naturally occurring calcite samples from southeastern Colorado.

B.

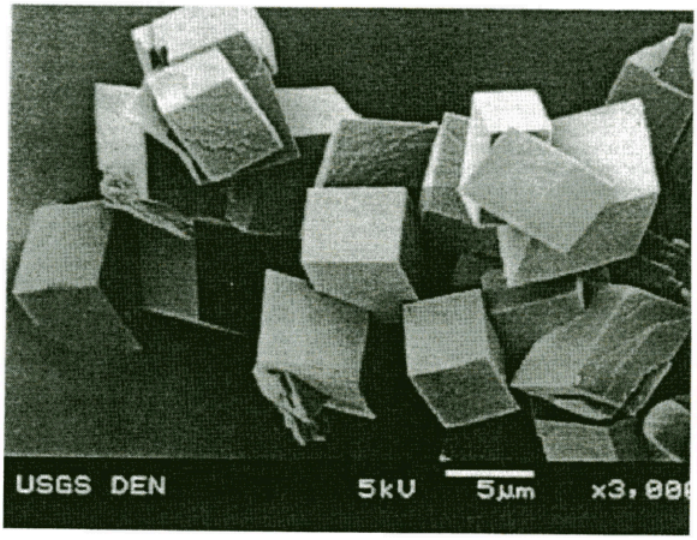

Fig. 8. (A) SEM photo of synthetic calcite (Baker) illustrating a lognormal CSD with large size variance (β^2 = 0.52). (B) SEM photo of synthetic calcite (CCNG-19) illustrating an Ostwald CSD with a small size variance (β^2 = 0.09).

Table 1. Summary of experimental methods and conditions for calcite crystal growth experiments.

Sample no.	CSD shapes	Initial vol. (mL)	Initial concentration (M)					Excess (mL)	Start	Final		Calculated	
			$CaCl_2$	$NaHCO_3$	Na_2CO_3	KNO_3	NaCl	$CaCl_2$ + KOH	pH[a]	pH	Duration	initial Ω	Final Ω
CCNG-2	asymptotic	150	0.0020	0.002		0.093		15	8.5	8.5	100 min	20	22.3
CCNG-30	asymptotic	300	0.0020	0.002		0.093		30	8.5	8.4	195 min	20	17.2
CCNG-35	lognormal	300	0.0020	0.002		0.093		30	8.8	8.7	140 min	30	24
CCNG-40	lognormal	300	0.0020	0.002		0.093		67	8.7	8.4	30 min[a]	40	19
CCNG-42	lognormal	300	0.0020	0.002		0.093		45	8.7	8.5	7 hours[a]	32	21
CCNG-43	lognormal	300	0.0020	0.002		0.093		33	8.6	8.5	230 min[a]	22	18
CCNG-44	lognormal	300	0.0020	0.002		0.093		32	8.6	8.5	5 hours	22	17
CCNG-45	lognormal	300	0.0020	0.002		0.093		64	8.8	8.5	225 min[a]	41	26
CCNG-9	Ostwald	100	0.0265	0.002	0.0244	0.046			10.7	10.0	~1 min	3090[c]	[b]
CCNG-13	Ostwald	100	0.0265	0.002	0.0244	0.046			10.7	8.4	14 hours	3090[c]	42
CCNG-19	Ostwald	400	0.0050		0.0050		0.50		10.5	10.0	40 min	106	67
CCNG-20	Ostwald	200	0.0265	0.002	0.0244	0.046			10.5	8.1	90.5 hours	3090[c]	2
CCP-4[d]	Ostwald	400	0.0020	0.002		0.093			8.5	8.5	45 hours	5	5
7-26	transitional	400	0.0025		0.0025	0.025	0.25		10.3	10.3	53 min	28.2	[b]
7-12	transitional	400	0.0038		0.0050	0.05	0.50		10.5	10.5	50 min	53.7	[b]
7-20	transitional	400	0.0050		0.0050	0.05	0.50		10.3	10.3	49 min	69.2	[b]
CCNG-25	bimodal		0.0050	0.005			0.50		9.9	9.7	105 min	51.4	10.5

[a] In lognormal experiments, the time listed is the time from highest pH to final sampling.
[b] Ca^{2+} concentration data not available for calculation.
[c] Actual value of omega does not exceed ~100 due to short induction time.
[d] Constant composition experiment using CCNG-19 crystals as seed.

Table 2. Crystal size distribution data and statistical evaluation for calcite crystal growth experiments; horizontal lines indicate continuous growth experiments.

CSD shape	Sample no.	α	β^2	Group size	Average size (nm)	Lognormal significance, χ^2 test
asymptotic	CCNG-30/2	8.45	0.64	1,500	6,420	NA
asymptotic	CCNG-30/3	8.78	0.68	1,700	8,864	NA
asymptotic	CCNG-2	7.60	0.52	1,000	2,585	NA
lognormal	CCNG-42/1	8.91	0.30	1,000	8,500	2.5–5
~lognormal	CCNG-42/2	9.49	0.27	2,000	14,870	<1
lognormal	CCNG-42/3	9.62	0.36	1,500	17,810	10–20
lognormal	CCNG-43/1	8.69	0.38	2,000	7,140	>20
lognormal	CCNG-43/2	9.00	0.49	2,000	10,320	1–5
lognormal	CCNG-43/3	9.61	0.38	2,000	17,853	>20
lognormal	CCNG-44/1	8.81	0.32	2,000	7,950	>20
lognormal	CCNG-44/2	9.49	0.23	2,000	14,800	>20
lognormal	CCNG-40	8.65	0.16	1,000	6,200	>20
lognormal	CCNG-45/3	9.33	0.25	2,700	12,690	10–20
lognormal	CCNG-35	9.03	0.32	2,000	9,770	>20
lognormal	Baker calcite	7.72	0.59	500	2,944	10–20
Ostwald	CCNG-9	9.14	0.10	1,500	9,359	NA
Ostwald	CCNG-13	10.20	0.09	3,000	28,080	NA
Ostwald	CCNG-19	9.01	0.09	1,000	8,522	NA
Ostwald	CCNG-20	9.50	0.08	2,000	13,792	NA
Ostwald	CCP-4	9.24	0.07	2,000	10,640	NA
transitional	7-26	9.40	0.31	2,000	13,953	NA
transitional	7-12	9.15	0.13	2,000	10,040	NA
transitional	7-20	9.65	0.24	2,000	17,294	NA
bimodal	CCNG-25	9.93	0.25	3,000	22,812	NA

NA = not applicable.